



Controllable construction of CNT-Interconnected liquid metal networks for thermal management

Gang Zhou^{a,1}, Lei Yao^{a,1}, Zuoxiang Xie^a, Urooj Kamran^b, Junwen Xie^{c,*}, Fei Zhang^{c,*}, Soo-Jin Park^{d,*}, Yinhang Zhang^{a,e,*}

^a Key Laboratory of Carbon Materials of Zhejiang Province, College of Chemistry and Materials Engineering, Wenzhou University, Wenzhou 325035, China

^b Institute of Advanced Machinery Design Technology, Korea University, 145 Anam-ro, Seongbuk-gu, Seoul 02841, Republic of Korea

^c School of Science and Engineering, The Chinese University of Hong Kong, Shenzhen 518172, Guangdong, the People's Republic of China

^d Department of Chemistry, Inha University, 100 Inharo, Incheon 22212, South Korea

^e Rui'an Graduate College of Wenzhou University, Wenzhou, Zhejiang 325206, China

ARTICLE INFO

Keywords:

Thermal conductivity
Electromagnetic interference shielding
Flame retardancy
Battery thermal management

ABSTRACT

Multifunctional portable devices for thermal management are crucial due to the development of small micro-electronic devices. Traditional polymer composite-based materials have limitations such as single functionality, high costs, and low fire resistance. In this study, a multifunctional liquid metal (LM)-interconnected carbon nanotube (CNT)/aramid nanofiber (ANF) film was fabricated via facile vacuum-assisted self-assembly approach, followed by compression. ANFs serve as interfacial binders between LM and CNTs via hydrogen bonding, while LM interconnects the adjacent CNT layers for fast thermal transport of phonons and electrons. The resulting composite films exhibited high bidirectional thermal conductivity (in-plane: 4.6 W/mK, through-plane: 1.1 W/mK), providing reliable cooling. Moreover, the as-fabricated films demonstrated excellent flame retardancy (20 s of burning), impressive Joule heating performance (200 °C at 3.5 V), and effective electromagnetic interference shielding (53 dB). This work provides an efficient method for fabricating multifunctional thermal management materials for microelectronic devices, battery thermal management, and artificial intelligence.

1. Introduction

Portable hardware devices are widely used for energy storage, sensing, and health care [1]. The requirements for portable hardware devices, particularly for the health care sector, include lightweight, excellent thermal conductivity, long-lasting Joule heating, and electromagnetic interference (EMI) shielding [2]. Recently, it has become critical to maintain a constant and comfortable temperature for both human beings and microelectronic devices, particularly under cold conditions [3]. Thus, thermal indoor heating has been widely used to keep human beings and electronic devices warm. However, its high energy consumption imposes significant pressure on the environment, making its practical application unsatisfactory. Moreover, thermal spreading is vital for electronic devices [4]. This is mainly because the reliability and life span of the devices will decrease if heat cannot be efficiently dissipated from them. Additionally, as minimized electronic devices, such as smartphones and laptops, become increasingly popular,

a mass of electromagnetic waves (EMWs) will be generated during their practical applications, endangering human health [5]. Therefore, to maintain a high-quality life, there is an urgent need for multifunctional portable hardware devices that can simultaneously exhibit excellent thermal conductivity to prolong the life span of electronic devices, energy-saving heating modes to maintain a comfortable temperature for humans and devices in cold areas, and outstanding EMI shielding ability to protect electronic devices and humans from EMW pollution.

Although traditional metal-based materials exhibit excellent EMI shielding properties and energy-saving Joule heating performance, they are unsuitable for portable hardware devices because of their high cost, high density, and low anticorrosion ability [6,7]. Carbon-based materials, such as carbon nanotubes (CNTs) and graphene, have been regarded as potential replacements for metal-based materials. In particular, CNTs have distinct advantages, such as a lightweight, excellent electrical conductivity, and outstanding anticorrosion ability [8,9]. Therefore, CNT-based materials exhibit outstanding EMI shielding

* Corresponding authors.

E-mail addresses: 221019105@link.cuhk.edu.cn (J. Xie), feizhang@tju.edu.cn (F. Zhang), sjpark@inha.ac.kr (S.-J. Park), bank0719@163.com (Y. Zhang).

¹ Gang Zhou and Lei Yao contributed equally to this work.

performance and Joule heating properties. For example, a CNT/aramid nanofiber (ANF) aerogel was fabricated using a facile freeze-drying method, and it exhibited both excellent EMI shielding performance (54.4 dB) and Joule heating properties (52.6 °C at a supplied voltage of 5 V) [10]. Furthermore, Zhang et al. fabricated a CNT@MXene/cellulose film using a facile dip-coating and spray-coating method, and the film exhibited an EMI shielding effectiveness (SE) of 32.6 dB and a Joule heating performance of 154 °C at a supplied voltage of 4 V [11]. Moreover, Fu et al. used ANFs as a template to fabricate CNT-based fiber aerogels, which delivered an EMI SE of 36 dB and a Joule heating performance of 100.2 °C at a supplied voltage of 5 V [12]. Although the aforementioned CNT-based materials with high electrical conductivity (10^3 - 10^6 S/m) exhibit both excellent EMI shielding performance and Joule heating properties, they cannot be used for the thermal management of microelectronic devices. This is mainly because of their poor thermal conductivity (0.202 W/mK) [13]. Their poor thermal conductivity is mainly due to CNT entanglement, which can generate numerous weak bonding junctions and cause high interfacial thermal resistance.

To address this issue, the interconnected strategy is used to improve the thermal conductivity of CNT-based materials. For example, Au-CNT and Pt-CNT interconnected networks were fabricated using a facile in-situ reduction method. After interconnection, the thermal conductivity of the CNT-based materials increased by 70% [14]. However, noble metals were used in this approach, making the fabrication process expensive and unsuitable for practical applications. To reduce the fabrication cost, the noble metals were replaced with graphite nanoplatelets (GNPs). The GNP-interconnected CNTs (GNPs-CNTs) were constructed using a high-temperature graphitization approach [13]. Although the thermal conductivity of the GNPs-CNTs increased from 0.3 W/mK to 10.9 W/mK, the approach was complex and energy-consuming.

In this study, we used an energy-saving, low-cost, and facile vacuum filtration approach to fabricate gallium based liquid metal (LM)-interconnected CNT/ANF (LM-CNT/ANF) composite films. Owing to its excellent thermal (33 W/mK) and electrical conductivity (10^6 S/m) [15,16], LM was used as an interconnected filler in this structure to replace traditional noble metals and enhance the thermal conductivity

of CNTs. Thus, the interconnected composite films exhibited an in-plane thermal conductivity of 4.6 W/mK and a through-plane thermal conductivity of 1.0 W/mK. Owing to the excellent electrical conductivity of the CNTs, the composite films exhibited outstanding EMI shielding performance (54 dB) and excellent Joule heating performance (200 °C at a supplied voltage of 3.5 V). In brief, this multifunctional composite film can provide excellent thermal management services to humans and microelectronic devices.

2. Results and discussion

2.1. Fabrication of the LM-CNT/ANF composite films

A top-down approach was used to dissociate the Kevlar fibers, as shown in Fig. 1. During the fabrication process, the macroscale Kevlar fibers were chemically exfoliated into nanofibers in a potassium hydroxide (KOH)/dimethyl sulfoxide (DMSO) solvent. This is mainly because the hydrogen bonds in the Kevlar fibers were weakened by the abstraction of KOH. Meanwhile, the surface negative charges of the ANFs, which originated from the electrostatic repulsion among the ANFs, were beneficial for stabilizing red dispersion (Fig. 1 inset). Fig. 2a shows the X-ray diffraction (XRD) patterns of the ANFs and Kevlar fibers. The characteristic peaks at 20.76°, 23.32°, 29.12°, and 39.7° correspond to the 110, 200, 004, and 006 crystal planes of the Kevlar fibers, respectively. The high crystallinity is mainly ascribed to the highly ordered arrangement of molecular chains and the abundance of hydrogen bonds in Kevlar. However, only a broad peak near 21° was observed in the ANFs, demonstrating that the crystal structures of the Kevlar fibers and the hydrogen bonds were destroyed. Overall, the red dispersion and XRD results confirm that the ANFs were successfully prepared.

After the successful preparation of the ANFs, LM-CNT/ANF composite films with different LM/CNT ratios were fabricated using a vacuum filtration method, followed by a compression treatment. The crystal structure of LM-CNTs/ANFs was characterized by XRD. The peaks at 20.76°, 26.64°, and 26.4° correspond to the characterized peaks of the ANFs, CNTs, and LM, respectively, confirming that the three components were successfully combined (Fig. 2b). As shown in Fig. 2c, the LM

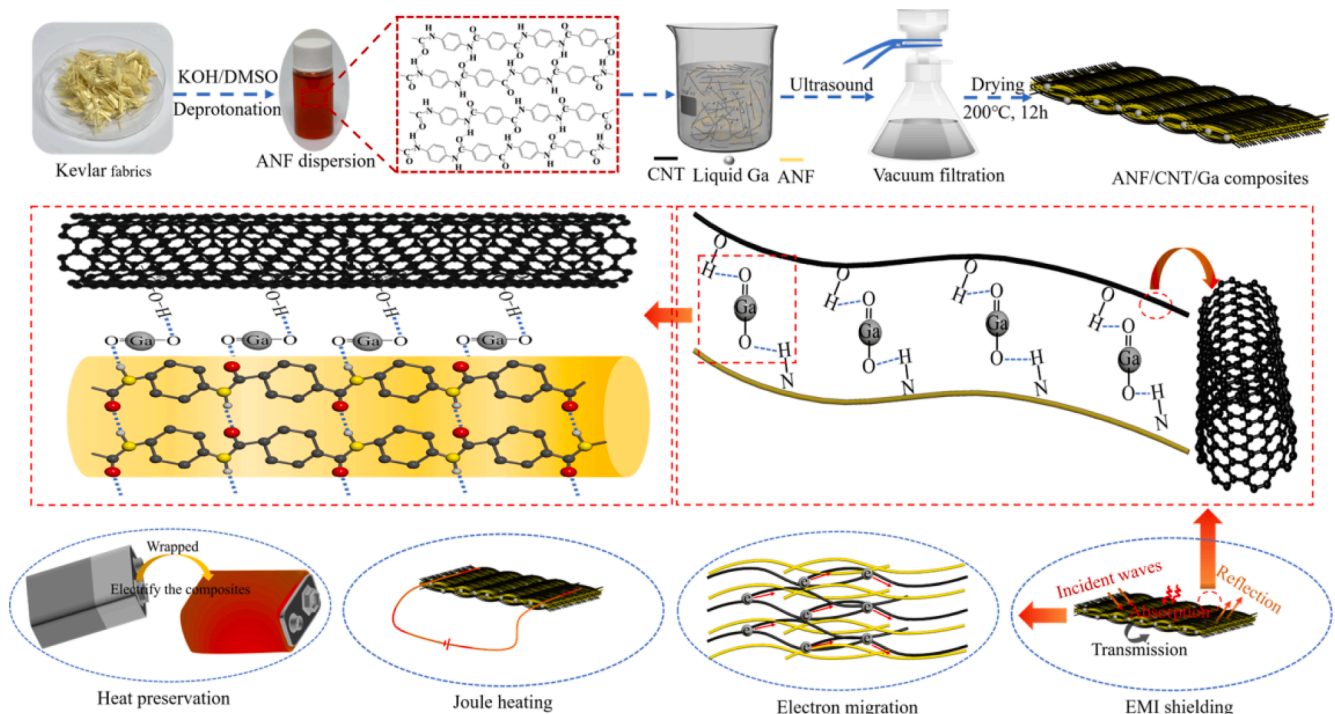


Fig. 1. Schematic of the fabrication of the LM-CNT/ANF composite films.

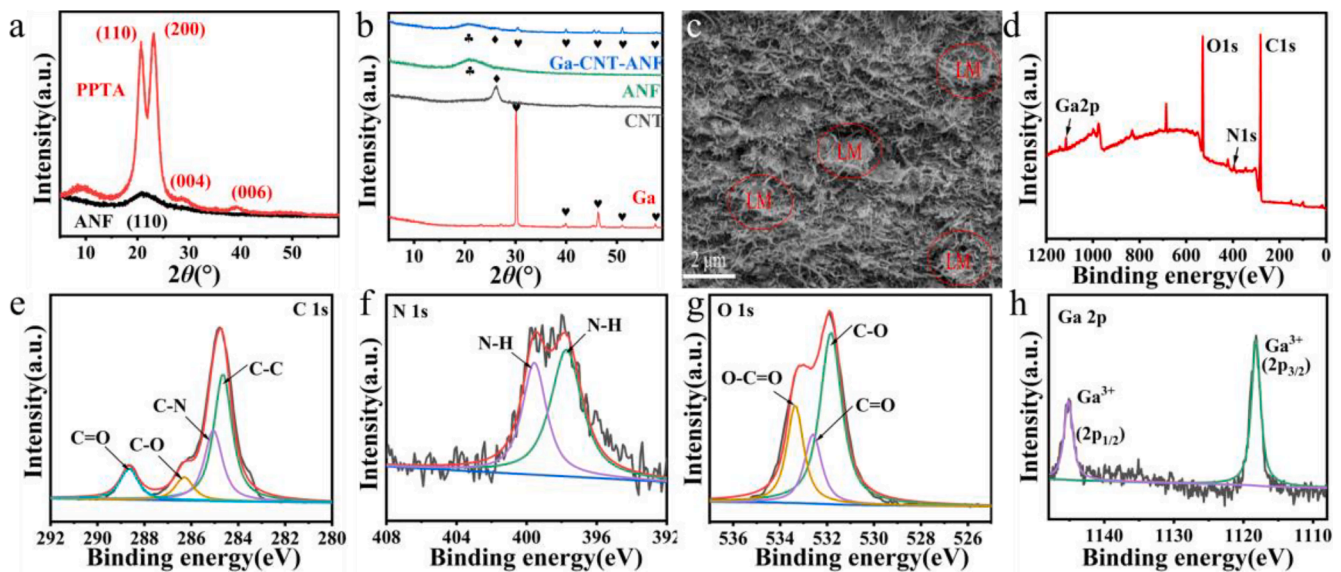


Fig. 2. (a) XRD pattern of the Kevlar fibers and ANFs. (b) XRD analysis of the pure CNT powders, pristine ANF film, Ga-based liquid metals, and LM-CNTs/ANFs. (c) SEM image of the LM-CNTs/ANFs. (d) XPS spectra of the LM-CNTs/ANFs. (e) High-resolution C 1s XPS spectrum of the LM-CNTs/ANFs. (f) High-resolution N 1s XPS spectrum of the LM-CNTs/ANFs. (g) High-resolution O 1s XPS spectrum of the LM-CNTs/ANFs. (h) High-resolution Ga 2p XPS spectrum of the LM-CNTs/ANFs.

particles were exhibited ellipsoidal structure due to the synergistic effect of gravity and negative pressure. Meanwhile, the ellipsoidal LM particles were gripped with CNTs and isolated from each other, thereby avoiding the coalescence of LM particles. The gripping effect of CNTs further confirmed the successful construction of the LM-CNT/ANF interconnected network. As shown in Fig. 2d, C, N, O, and Ga elements were detected in the LM-CNT/ANF film, further demonstrating the successful combination of the three components. The high-resolution C 1s, N 1s, O 1s, and Ga 2p spectra are shown in Fig. 2e, 2f, 2g, and 2h, respectively, to characterize the functional groups of the LM-CNT/ANF composite film. The C 1s spectrum is fitted by four peaks at 288.8 eV, 286.5 eV, 285.1 eV, and 284.8 eV, which correspond to C=O, C-O, C-N, and C-C, respectively [17]. Additionally, the N 1s spectrum could be separated into two peaks at 400 eV and 397.8 eV, both of which correspond to N-H [18]. Moreover, the O 1s spectrum was deconvoluted into three peaks at 533.8 eV, 532.8 eV, and 531.7 eV, which correspond to O-C=O, C=O, and C-O, respectively [19]. This confirms that the LM-CNT/ANF composite films contained numerous polar functional groups and hydrogen bonds, which could provide ample interactions among the different components. Furthermore, the high-resolution Ga 2p X-ray photoelectron spectroscopy (XPS) spectrum of the LM-CNT/ANF film exhibited a strong Ga³⁺ peak. This demonstrates that Ga₂O₃ is the main component of the LM surface [20]. Overall, the successful integration of the LM, CNTs, and ANFs was validated by XRD and XPS.

2.2. Thermal conductivity and flame retardancy of the LM-CNT/ANF composite films

The thermal conductivity of the LM-CNT/ANF composite film was characterized using the laser flash approach. Fig. 3a and 3b show both the in-plane and through-plane thermal conductivities of the LM-CNTs/ANFs with various LM/CNT ratios. As the LM content increased, both the in-plane and through-plane thermal conductivities increased. When the LM/CNT ratio was 6:3, both the in-plane and through-plane thermal conductivities reached their maximum values (in-plane thermal conductivity: 4.6 W/mK and through-plane thermal conductivity: 1.1 W/mK). This is mainly because a high LM content allowed for the construction of more interconnected networks to enhance thermal conductivity. Conversely, a low LM content allowed for the construction of limited interconnected networks to provide continuous thermal conductive pathways, which is ascribed to the large phonon scattering

among the CNT junctions [21].

The LM-CNT/ANF film was used to cool an LED chip (80 W) in order to demonstrate its heat-dissipating capability. A pristine ANF film and the LM-CNT/ANF film (CNTs:LM = 3:6) were inserted between the top LED chip and the bottom foam to serve as thermal management materials (TMMs). The variations in the surface temperature of the LED modulus over time were recorded by an infrared thermal camera (Fig. 3c), and the experimental images of the TMMs are exhibited in Fig. 3d. When the pristine ANF film was used as a heat dissipater, the surface temperature of the LED chip rapidly increased to 132 °C within 30 s. However, the surface temperature of the LM-CNT/ANF film only reached 115 °C within the same operating time and was significantly lower than that of the pristine ANF film. The life span of LED chips is well known to exponentially depend on the operating temperature. Once the working temperature of LED chips decreases by 10 °C, their lifetime will be prolonged by 50%. Consequently, the LM-CNT/ANF film with excellent bidirectional thermal conductivity and low manufacturing cost has great potential for use in high-power electronic devices.

Flame retardancy is crucial for multifunctional portable hardware devices, which are used in TMMs. Thus, a flame exposure measurement was performed to characterize the flame-retardant properties of the pristine ANF film and the LM-CNT/ANF film. When the pristine ANF film was ignited by an alcohol lamp, it burned out rapidly and heavily and continued burning for 20 s. However, the LM-CNT/ANF film slightly burned without melt-dripping during the whole combustion process. After 20 s of burning, the integrity of the LM-CNT/ANF film could be maintained, demonstrating that the film has outstanding flame-retardant properties due to the excellent flame retardancy of LM and CNTs. Once the composite films are exposed to fire, it can be expected that the CNTs have intrinsic non-flammable property [22]. In addition, the heat originated from fire can be absorbed by the Ga based liquid metal. Meanwhile, the surface oxide layer of LM can act as barrier to hinder the penetration of oxygen to slow down the combustion and the metallic core of LM can terminate the reactions of free radicals to delay the combustion [23,24]. Moreover, the LM-b-CNT composite films have excellent in-plane thermal conductivity to dissipate the heat.

2.3. Joule heating and battery thermal management of the LM-CNT/ANF film

Fig. 4 describes the Joule heating performance of the LM-CNTs/

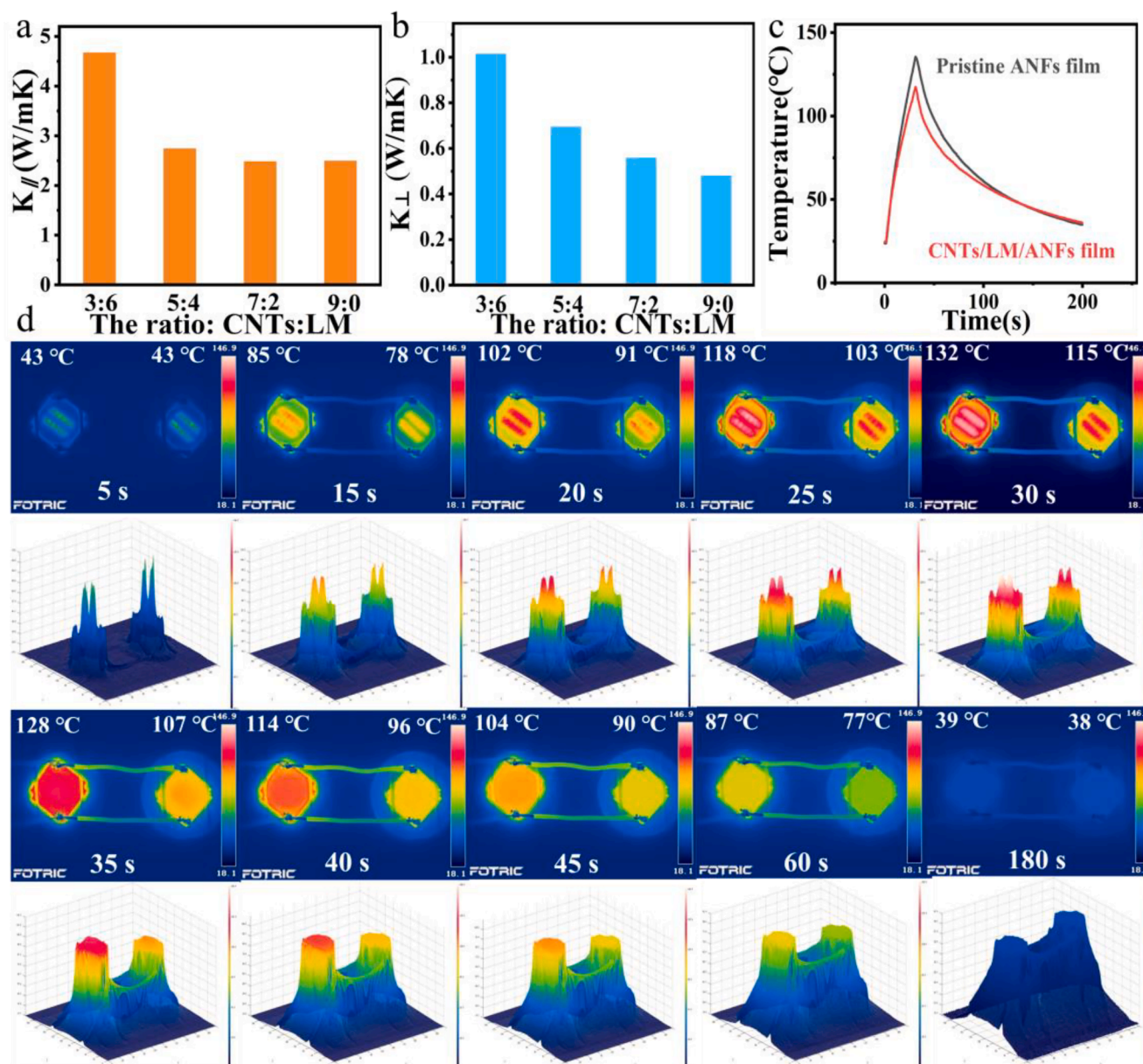


Fig. 3. (a) Through-plane thermal conductivity of the LM-CNT/ANF films with different LM/CNT ratios. (b) In-plane thermal conductivity of the LM-CNT/ANF film with different LM/CNT ratios. (c) Variations in the surface temperature of the LM-CNT/ANF film. (d) Thermal infrared images of the LED chips using two TMMs (the pristine ANF film and the LM-CNT/ANF film).

ANFs. Fig. 4a indicates the current–voltage plot of the LM-CNTs/ANFs, which demonstrates how well the hybrid films follow Ohm’s law and suggests that the composite films have a low sheet resistance (6.25 Ω /sq). The low sheet resistance can provide low-driven voltage Joule heating performance and protect humans from empyrosis. Fig. 4b shows the temperature–time curve, which suggests that the saturated temperature can be easily adjusted by tuning the driven voltages. Meanwhile, the saturated temperature increases as the stimuli voltages increase. Once the driven voltage is as low as 1.5 V, the saturated temperature can reach 55 °C. This temperature is suitable for thermal therapy. As the voltage increases to 2, 2.5, 3, and 3.5 V, the saturated temperature can reach 80 °C, 112 °C, 152 °C, and 198 °C, respectively. Once the external electric sources are turned off, the surface temperature of the materials can rapidly decrease to the ambient temperature. An infrared thermal camera can be used to obtain the visual feedback of the Joule heating property. Fig. 4c depicts the color variation of the LM-CNTs/ANFs from blue to red. Fig. 4d shows how the surface temperature of the materials

could be easily and conveniently regulated owing to their high sensitivity toward Joule heating. The materials in this study have a better Joule heating temperature than previously reported Joule heating materials (Fig. 4e). Fig. 4f and 4g show the long-term Joule heating measurement results. Fig. 4f reveals that the hybrid film can stably experience increasing and decreasing surface temperatures at an external voltage of 2.5 V for 20 cycles. Fig. 4g shows that the hybrid films can maintain a steady saturated temperature of 125 °C for 3000 s at a supplied voltage of 2.5 V. Overall, both Fig. 4f and 4g confirm that the hybrid films can exhibit excellent Joule heating performance with high reliability and repeatability. Therefore, the hybrid films may be regarded as outstanding candidates for the next generation of wearable thermal therapy devices.

The LM-CNT/ANF films can be used for personal thermal management, deicing, and battery thermal management because of their excellent Joule heating performance. Their surface temperature can increase to 66 °C within 60 s at a low supplied voltage of 2 V. Since this

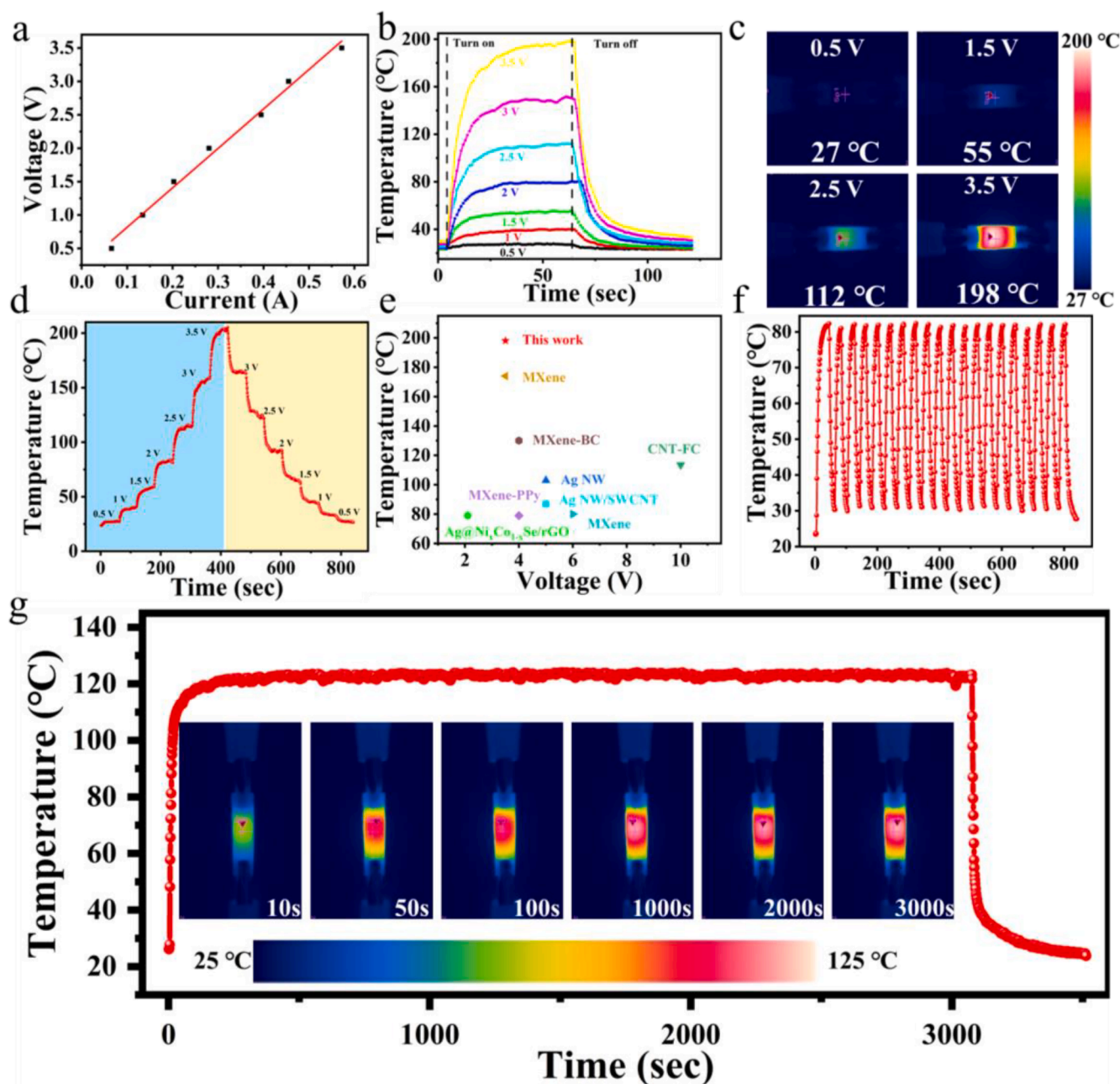


Fig. 4. (a) Current–voltage characteristics of the LM-CNT/ANF film. (b) Surface temperatures of the LM-CNT/ANF film versus time at various supplied voltages. (c) Infrared images of the surface temperature of the LM-CNT/ANF film versus time at various supplied voltages. (d) Joule heating performance of the LM-CNT/ANF film at gradient voltages. (e) Comparison between the Joule heating performance of the LM-CNT/ANF film and that of other reported Joule heating materials [2,6,10,25–29]. (f) Joule heating performance of the LM-CNT/ANF film during cyclic on/off measurements. (g) Long-term Joule heating performance of the LM-CNT/ANF film at 2.5 V.

temperature can accelerate blood circulation to relieve arthritis pain or reduce muscle stiffness, the LM-CNT/ANF films can be used as wearable heaters to heat the knee, wrist, and elbow (Figure S2) [30]. Moreover, a deicing experiment was implemented to test the deicing ability of the LM-CNT/ANF film. The LM-CNT/ANF film melted 5 cm³ of the ice in 28 min at a low voltage of 2 V, and the final temperature of the water reached 40 °C (Figure S3). Hence, the LM-CNT/ANF film may be considered an excellent candidate for minimizing the threat of ice accretion.

Most countries are located in high-latitude regions, where the annual average temperature is below 0 °C [31]. Electric vehicles easily drop in this cold environment because commercial Li-ion batteries (LIBs) cannot normally work in this environment owing to sluggish kinetics. An

increase in internal resistance, capacity loss, and even the growth of Li dendrites are caused by sluggish kinetics [32]. Even worse, the Li dendrites will easily break the battery separators, causing the batteries to be short-circuited and even posing threats to personal safety [33,34]. To address these problems, the batteries must operate at temperatures of 30–40 °C, which necessitates the use of highly efficient Joule heating materials to heat the batteries. Therefore, the LM-CNT/ANF film with an excellent Joule heating performance can be used as TMMs to enable batteries operate at optimal temperatures (30–40 °C).

Two commercial 18,650 LIBs were placed in a cold environment with a temperature of about 0 °C. One was heated by the LM-CNT/ANF film (Fig. 5a), and the other had no package. Subsequently, a low voltage (1.5 V) was applied to the LM-CNT/ANF film to heat the battery via

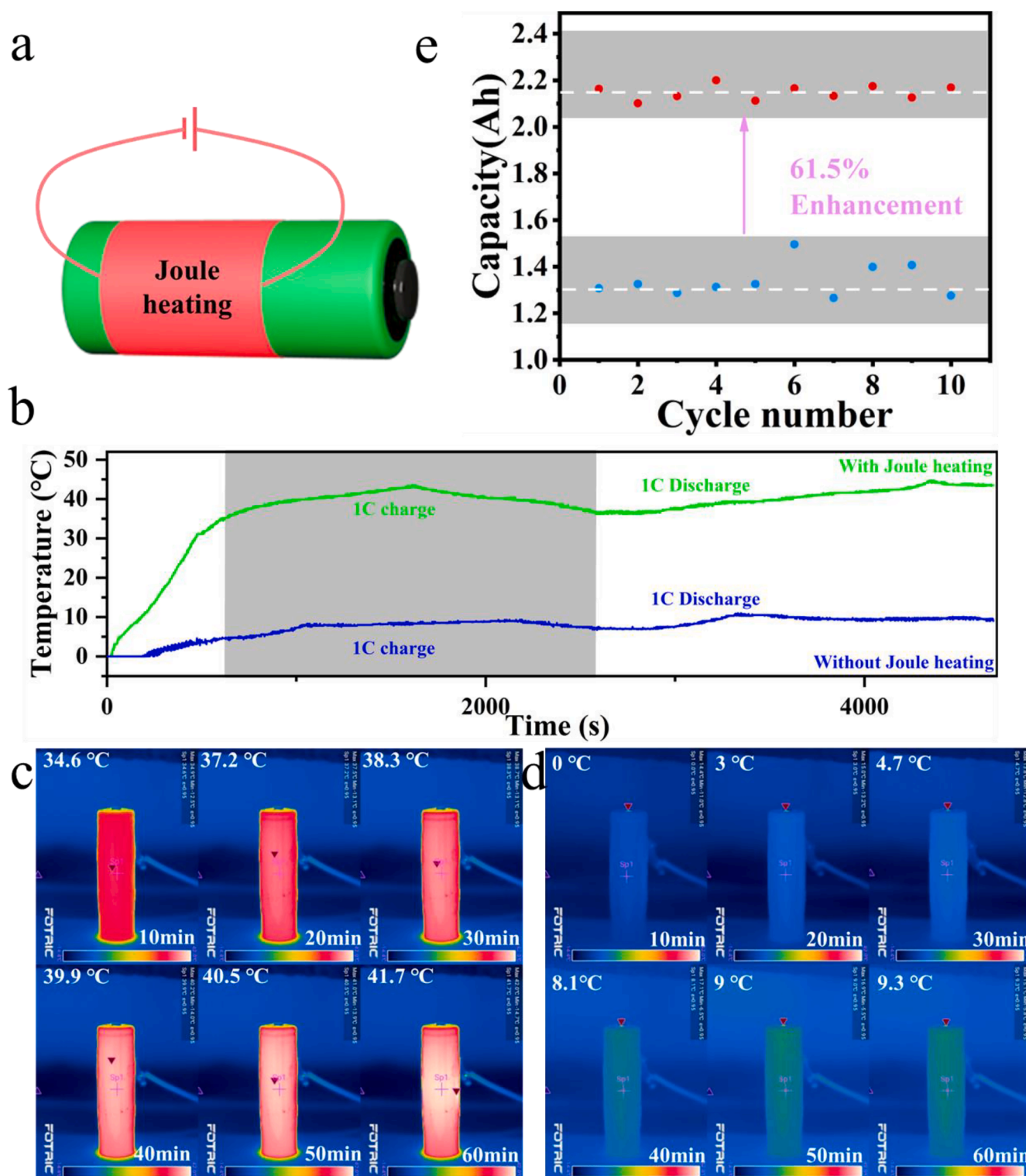


Fig. 5. (a) Demonstration of the battery being heated by the LM-CNT/ANF film. (b) Surface temperatures of the batteries with and without Joule heating materials over time in a cold environment. (c) Infrared thermal images of the battery with and without Joule heating during the entire 1C charge/discharge process. (d) Capacity comparison of the batteries with and without Joule heating in a cold environment.

Joule heating before the initiation of a 1C discharge/charge process. Fig. 5b depicts the temperature–time plot for the LIBs packed with and without the LM-CNT/ANF film, and Fig. 5c and 5d show the corresponding infrared thermal images. The surface temperature of the LIB wrapped with the LM-CNT/ANF film could be dramatically increased from 0 °C to 30 °C within 600 s, and it stabilized at around 30–40 °C during the continuous 1C charge/discharge process (Fig. 5c). However,

under the same condition, the operating temperature of the LIB without any package ranged from 0 °C to 10 °C, which is far lower than the optimal working temperature (Fig. 5d). Consequently, the capacity of the LIB heated by the LM-w-GNP/ANF film increased by 61.5% when compared to that of the LIB without Joule heating (Fig. 5e).

2.4. EMI shielding performance of the LM-CNT/ANF film

The EMI shielding properties of the LM-CNT/ANF films with different CNT/LM ratios were analyzed using a vertical analyzer network, and their corresponding total SE (SE_T) values are shown in Fig. 6a. Except for that of the film with a ratio of 3:6, the SE_T of the film with other ratios surpassed the commercial standard (20 dB) in the X band (8.2–12.4 GHz). Specifically, the film with a ratio of 7:2 had a higher SE_T value (53 dB) than the films with other ratios. Additionally, as the LM content increased, the SE_T of the materials first increased and then decreased, finally peaking at 20 wt% LM. This may be because a small LM content can exert an interconnected effect to bridge adjacent CNTs and create continuous electrically conductive paths, resulting in enhanced EMI shielding performance, compared to no LM content. Once the LM content surpasses 20 wt%, the EMI shielding capability decreases, which may be mainly because the electrically conductive paths are destroyed by the LM. Thus, the sample with 20 wt% LM had the best EMI shielding property. Moreover, both the microwave absorption (SE_A) and microwave reflection (SE_R) exhibit the same trend as the SE_T (Fig. 6b). Fig. 6b also indicates that all the SE_A values are higher than the

SE_R values, indicating that the LM-/CNTs/ANFs have a strong EMW absorption ability. The power coefficients of the different materials, such as absorption (A), reflection (R), and transmission (T), are presented in Fig. 6c to further analyze the EMI shielding mechanism. The above parameters can describe the absorption, reflection, and transmission capability of EMI shielding materials toward EMWs. Figure indicates that the T values of all the materials with different ratios were as low as 10^{-3} , illustrating that both the LM-CNTs/ANFs and CNTs/ANFs can shield 99.999% EMWs. Meanwhile, the R values of all the samples were considerably higher than their A values. This implies that although the composite materials have excellent EMW absorption ability, their dominant shielding mechanism is reflection. The LM-CNTs/ANFs have the highest EMI shielding performance among all the reported shielding materials (Fig. 6d). Moreover, thickness and density are two critical parameters for assessing the EMI shielding property of the materials. The ratio of SE values to thickness (SSE) and the ratio of SE values to thickness and density (SSE_t) are used to analyze the contributions of thickness and density to SE values, respectively. Equations (7) and (8) express the detailed SSE and SSE_t definitions, respectively. Both the SSE and SSE_t values of the LM-CNTs/ANFs are higher than

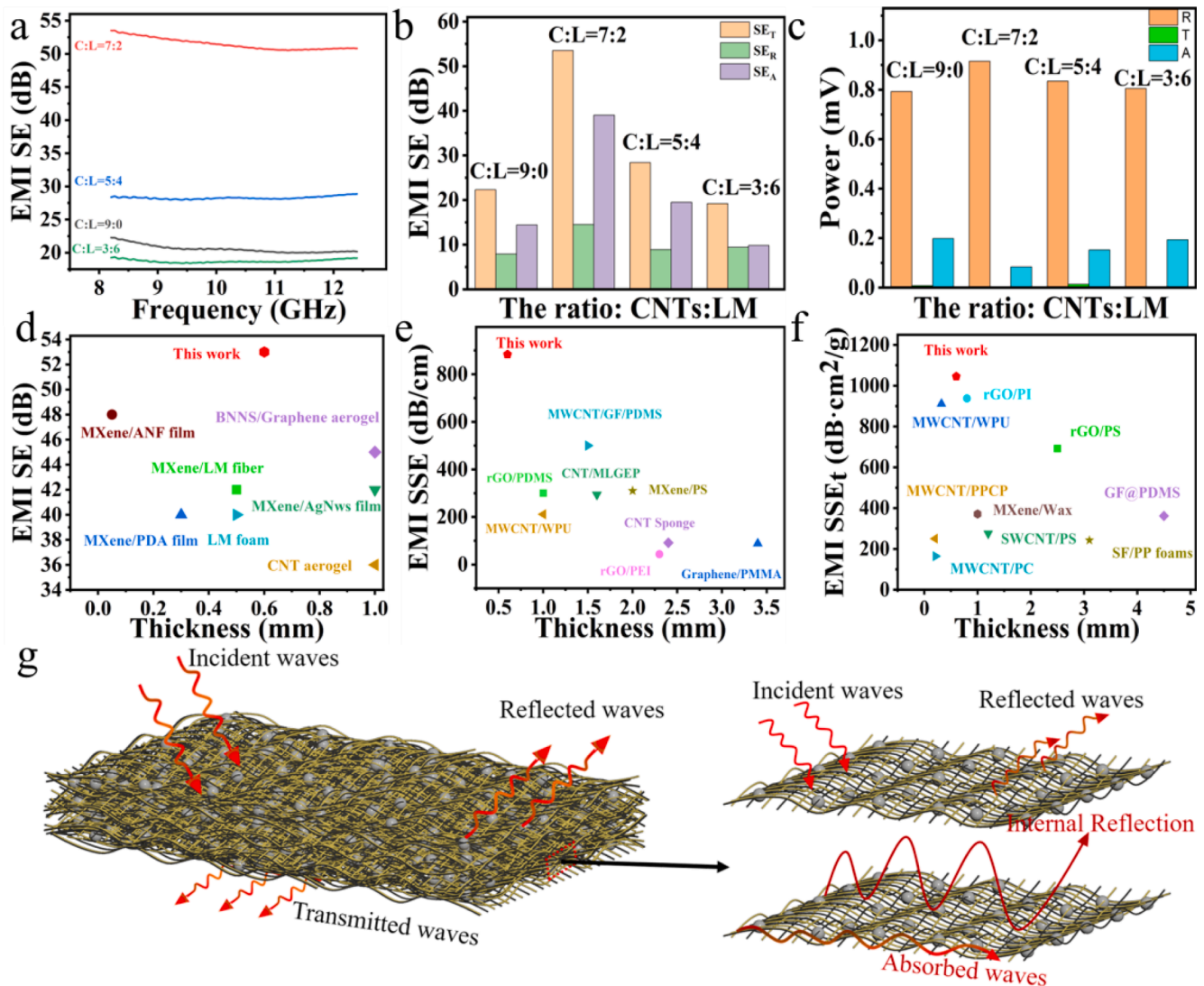


Fig. 6. (a) EMI SE of the LM-CNT/ANF film. (b) Average SE_T , SE_R , and SE_A of the LM-CNT/ANF film with different CNT/LM ratios. (c) Average R, A, and T of the LM-CNT/ANF film with different CNT/LM ratios. (d) Comparison of the EMI SE versus thickness of the LM-CNTs/ANFs to that of other shielding materials such as carbon-based, conductive polymer, and MXene-based materials in the X-band [3,12,19,40–43]. (e) Comparison of the SSE versus thickness of the LM-CNTs/ANFs to that of previously reported EMI materials [44–52]. (f) Comparison of the SSE_t versus thickness of the LM-CNTs/ANFs to that of previously reported EMI materials [51,53–60].

those of reported materials, as shown in Fig. 6e and 6f. This further confirms that the fabricated LM-CNTs/ANFs may have significant application potential in military, aerospace, and artificial intelligence.

Fig. 6g shows the detailed EMI shielding mechanism of the LM-CNTs/ANFs. When EMWs encounter the surface of the materials, a mass of EMWs can be reflected owing to the strong reflection ability of CNTs [35]. Meanwhile, the residual EMWs are transferred into the hybrid film, and then they can be dissipated by the induced currents [36]. This is mainly because CNTs with high electrical conductivity can mitigate and hop electrons, causing conductive loss to attenuate the energy of the EMWs [37]. Furthermore, the EMWs can be dissipated by interfacial polarization induced by several interfaces. These interfaces include the interfaces between the conductive CNTs and the insulated ANFs, the conductive core (Ga) and the insulated LM shell (Ga_2O_3), and the conductive CNTs and Ga_2O_3 . Additionally, several edges and defects on the crystal structures of CNTs can contribute to EMI shielding [38,39]. This could be because a mass of several dipolar polarizations originating from these structures can cause dielectric loss to attenuate the EMWs. Eventually, the hybrid structures provide several surfaces for multiple reflections to scatter the EMWs until they are completely absorbed.

Figure S4 depicts the LM-w-GNP/ANF films during practical EMI shielding applications. The electromagnetic radiation values were detected by an electromagnetic radiation tester (LZT-1130). When the LM-w-GNP/ANF film with a diameter of 4 cm was placed between the socket and the tester, the value decreased from 440 mw/cm^2 to 41 mw/cm^2 , indicating its outstanding EMI shielding performance.

3. Conclusions

In summary, LM-CNT/ANF films were fabricated using a facile vacuum filtration method, followed by mechanical compression. The interconnected network of the LM-CNTs contributes to the construction of bidirectional pathways, which enhance the transport of phonons and electrons between the adjacent CNT layers. The fabricated composite film exhibited excellent bidirectional thermal conductivities (in-plane: 4.6 W/mK and through-plane: 1.1 W/mK), excellent Joule heating performance ($200 \text{ }^\circ\text{C}$ at a supplied voltage of 3.5 V), and outstanding EMI properties (EMI SE: 53 dB). The resultant multifunctional LM-w-GNP/ANF film not only expands knowledge of the interconnected strategy but also provides promising application opportunities, including efficient thermal management, flame retardant, Joule heating, and EMI shielding.

4. Experimental section

4.1. Materials

Carboxylated CNTs (CNTs-COOH) were purchased from Jiangsu Xianfeng Nanomaterial Technology Co., Ltd., China. Ga-based LMs (99.99% metal basis) were supplied by Macklin. Aramid fibers with a diameter of $7 \text{ }\mu\text{m}$ were purchased from Dongguan Yueshun New Materials Ltd. DMSO ($\geq 99.8\%$, GC) and KOH ($\geq 99.99\%$) were provided by Macklin.

4.2. Fabrication of the LM-CNT/ANF films

Aramid microfibers were exfoliated using a deprotonation method to fabricate the ANFs (Kevlar fibers). Briefly, 0.8 g of aramid fibers (with a diameter of $7 \text{ }\mu\text{m}$) and 1.2 g of KOH were introduced into 400 mL of DMSO. The obtained aramid fiber/KOH/DMSO suspension was magnetically stirred at 1000 rpm and $25 \text{ }^\circ\text{C}$ for 72 h . The resultant ANF dispersions had a 2 mg/mL concentration and were dark red.

To fabricate LM/DMSO dispersions, 0.9 g of Ga-based LM was dropped into 300 mL of the DMSO solvent. Uniform LM/DMSO dispersions with a concentration of 3 mg/mL were obtained via

ultrasonication for 20 min . Subsequently, LM/CNT/DMSO mixture solutions with various LM/CNT ratios were prepared and mixed with the ANF dispersions under 1000 rpm magnetic stirring for 20 min and sonication for 15 min . DI water was slowly added to the mixture solution because the protonation process of ANFs produces a significant amount of heat. Finally, pristine ANF films and LM-CNT/ANF composite films were fabricated using the vacuum filtration approach and nylon filter membranes with a $0.22 \text{ }\mu\text{m}$ diameter. All the filtered films were rinsed with DI water eight times and then dried in a vacuum oven at $60 \text{ }^\circ\text{C}$ overnight to remove DMSO. After drying, the dried composite films were peeled off and placed between two pieces of PTFE membranes to be compressed under 100 MPa for 5 min .

4.3. Characterization

The morphology of the LM-CNTs/ANFs was characterized using a TESCAN SOLARIS scanning electron microscope. The specific heat capacity (C_p) was determined using a differential scanning calorimeter (TAQ 20 DSC). The densities (ρ) of the samples were determined by dividing the mass by the volumes. The thermal diffusivity (α) was determined using a laser flash analyzer (LFA 447). The thermal conductivity (K) was obtained using the formula $K = \alpha \times C_p \times \rho$. The heat dissipation measurement was validated by employing an infrared camera (E95, FLIR) to record the surface temperatures of the LM-CNT/ANF and pristine ANF films during the heating and cooling processes. The crystal structures of the ANF and LM-CNT/ANF films were determined by XRD (Rigaku, SmartLab X-ray diffractometer) at a scanning range of 5° – 80° and a scanning rate of $20^\circ \text{ min}^{-1}$. The sample components were characterized by XPS using an AXIS Supra instrument (Kratos Analytical, Japan). The surface temperature of the LM-w-GNP/ANF film was recorded with a paperless recorder (KSB1-24AOR, Ningbo, China), and the corresponding infrared images were captured by the infrared camera (E95, FLIR). Various voltages of 0.5 – 3.5 V were supplied by an M8813 150 V/1A Maynuo DC Source Meter. The EMI parameters (i.e., S_{11} , S_{12} , S_{21} , and S_{22}) of the different samples were measured by the vector network analyzer (Agilent E5071C) in the X-band. The SE_T , SE_R , SE_A , specific effectiveness (SSE), and SSE/t values were calculated using the following equations:

$$R = |S_{11}|^2 \quad (1)$$

$$T = |S_{21}|^2 \quad (2)$$

$$A = 1 - R - T \quad (3)$$

$$SE_R = -10 \times \log(1 - R) \quad (4)$$

$$SE_A = -10 \times \log\left(\frac{T}{1 - R}\right) \quad (5)$$

$$SE_T = -10 \times \log(T) = SE_R + SE_A \quad (6)$$

$$SSE = \frac{SE}{thickness} = dB \times cm^{-1} \quad (7)$$

$$SSE_t = \frac{SSE}{density} = dB/cm \times g \quad (8)$$

where R , T , and A represent the EM reflection, EM transmission, and EM absorption coefficients, respectively.

Declaration of Competing Interest

The authors declare that they have no known competing financial interests or personal relationships that could have appeared to influence the work reported in this paper.

Data availability

The data that has been used is confidential.

Acknowledgements

This work was supported in part by the National Natural Science Foundation of China (Grant No. 52302045), the Basic Scientific Research Projects of Wenzhou City (Grant No. G20220018), Zhejiang Xinmiao Talents Program (Grant No. 2023R451024), the National Research Foundation of Korea (NRF) grant funded by the Korea government (MSIT) (No. 2023R1A2C1004109).

Appendix A. Supplementary material

Supplementary data to this article can be found online at <https://doi.org/10.1016/j.compositesa.2023.107743>.

References

- Dubal DP, Chodankar NR, Kim DH, Gomez-Romero P. Towards flexible solid-state supercapacitors for smart and wearable electronics. *Chem Soc Rev* 2018;47:2065–129.
- Zhou Z, Song Q, Huang B, Feng S, Lu C. Facile Fabrication of Densely Packed Ti3C2 MXene/Nanocellulose Composite Films for Enhancing Electromagnetic Interference Shielding and Electro-/Photothermal Performance. *ACS Nano* 2021.
- Wang J, Ma X, Zhou J, Du F, Teng C. Bioinspired, High-Strength, and Flexible MXene/Aramid Fiber for Electromagnetic Interference Shielding Papers with Joule Heating Performance. *ACS Nano* 2022;16:6700–11.
- Huang C, Qian X, Yang R. Thermal conductivity of polymers and polymer nanocomposites. *Mater Sci Eng R Rep* 2018;132:1–22.
- Iqbal A, Sambyal P, Koo CM. 2D MXenes for Electromagnetic Shielding: A Review. *Adv Funct Mater* 2020;30.
- Ma Z, Kang S, Ma J, Shao L, Wei A, Liang C, et al. High-Performance and Rapid-Response Electrical Heaters Based on Ultraflexible, Heat-Resistant, and Mechanically Strong Aramid Nanofiber/Ag Nanowire Nanocomposite Papers. *ACS Nano* 2019;13:7578–90.
- Zhou B, Su M, Yang D, Han G, Feng Y, Wang B, et al. Flexible MXene/Silver Nanowire-Based Transparent Conductive Film with Electromagnetic Interference Shielding and Electro-Photo-Thermal Performance. *ACS Appl Mater Interfaces* 2020;12:40859–69.
- Wan YJ, Wang XY, Li XM, Liao SY, Lin ZQ, Hu YG, et al. Ultrathin Densified Carbon Nanotube Film with “Metal-like” Conductivity, Superior Mechanical Strength, and Ultrahigh Electromagnetic Interference Shielding Effectiveness. *ACS Nano* 2020;14:14134–45.
- Wang H, Zhou R, Li D, Zhang L, Ren G, Wang L, et al. High-Performance Foam-Shaped Strain Sensor Based on Carbon Nanotubes and Ti(3)C(2)T(x) MXene for the Monitoring of Human Activities. *ACS Nano* 2021;15:9690–700.
- Hu P, Lyu J, Fu C, Gong WB, Liao J, Lu W, et al. Multifunctional Aramid Nanofiber/Carbon Nanotube Hybrid Aerogel Films. *ACS Nano* 2020;14:688–97.
- Zhang Y, Wang W, Xie J, Dai K, Zhang F, Zheng Q. Smart and flexible CNTs@MXene heterostructure-decorated cellulose films with excellent electrothermal/photothermal conversion and EMI shielding performances. *Carbon* 2022;200:491–9.
- Fu C, Sheng Z, Zhang X. Laminated Structural Engineering Strategy toward Carbon Nanotube-Based Aerogel Films. *ACS Nano* 2022;16:9378–88.
- Zhang F, Feng Y, Qin M, Gao L, Li Z, Zhao F, et al. Stress Controllability in Thermal and Electrical Conductivity of 3D Elastic Graphene-Crosslinked Carbon Nanotube Sponge/Polyimide Nanocomposite. *Adv Funct Mater* 2019;29:1901383.
- Qiu L, Zou H, Wang X, Feng Y, Zhang X, Zhao J, et al. Enhancing the interfacial interaction of carbon nanotubes fibers by Au nanoparticles with improved performance of the electrical and thermal conductivity. *Carbon* 2019;141:497–505.
- Gao Y, Liu J. Gallium-based thermal interface material with high compliance and wettability. *Appl Phys A* 2012;107:701–8.
- Sun Y, Han X, Guo P, Chai Z, Yue J, Su Y, et al. Slippery Graphene-Bridging Liquid Metal Layered Heterostructure Nanocomposite for Stable High-Performance Electromagnetic Interference Shielding. *ACS Nano* 2023;17:12616–28.
- Yin L, Zhang B, Tian M, Ning N, Zhang L, Wang W. Surface construction of ANF/CNT onto aramid fibers to enhance interfacial adhesion and provide real-time monitoring of deformation. *Compos Sci Technol* 2022;223.
- Yang B, Wang L, Zhang M, Luo J, Ding X. Timesaving, High-Efficiency Approaches To Fabricate Aramid Nanofibers. *ACS Nano* 2019;13:7886–97.
- Yi P, Zou H, Yu Y, Li X, Li Z, Deng G, et al. MXene-Reinforced Liquid Metal/Polymer Fibers via Interface Engineering for Wearable Multifunctional Textiles. *ACS Nano* 2022;16:14490–502.
- Yu D, Liao Y, Song Y, Wang S, Wan H, Zeng Y, et al. A Super-Stretchable Liquid Metal Foamed Elastomer for Tunable Control of Electromagnetic Waves and Thermal Transport. *Adv Sci (Weinh)* 2020;7:2000177.
- Guo H, Liu J, Wang Q, Liu M, Du C, Li B, et al. High thermal conductive poly(vinylidene fluoride)-based composites with well-dispersed carbon nanotubes/graphene three-dimensional network structure via reduced interfacial thermal resistance. *Compos Sci Technol* 2019;181.
- F. Chen, Y. Huang, R. Li, S. Zhang, Q. Jiang, Y. Luo, B. Wang, W. Zhang, X. Wu, F. Wang, P. Lyu, S. Zhao, W. Xu, F. Wei, R. Zhang, Superdurable and fire-retardant structural coloration of carbon nanotubes, *Science Advances* 8 eabn5882.
- Wang H, Xing W, Chen S, Song C, Dickey MD, Deng T. Liquid Metal Composites with Enhanced Thermal Conductivity and Stability Using Molecular Thermal Linker. *Adv Mater* 2021;33:e2103104.
- Li X, Li M, Shou Q, Zhou L, Ge A, Pei D, et al. Liquid Metal Initiator of Ring-Opening Polymerization: Self-Capsulation into Thermal/Photomoldable Powder for Multifunctional Composites. *Adv Mater* 2020;32:e2003553.
- Hazarika A, Deka BK, Jeong C, Park YB, Park HW. Biomechanical Energy-Harvesting Wearable Textile-Based Personal Thermal Management Device Containing Epitaxially Grown Aligned Ag-Tipped-NixCo1–xSe Nanowires/Reduced Graphene Oxide. *Adv Funct Mater* 2019;29.
- Kim H, Seo M, Kim JW, Kwon DK, Choi SE, Kim JW, et al. Highly Stretchable and Wearable Thermotherapy Pad with Micropatterned Thermochromic Display Based on Ag Nanowire–Single-Walled Carbon Nanotube Composite. *Adv Funct Mater* 2019;29.
- Liu X, Jin X, Li L, Wang J, Yang Y, Cao Y, et al. Air-permeable, multifunctional, dual-energy-driven MXene-decorated polymeric textile-based wearable heaters with exceptional electrothermal and photothermal conversion performance. *J Mater Chem A* 2020;8:12526–37.
- Shi M, Shen M, Guo X, Jin X, Cao Y, Yang Y, et al. Ti3C2Tx MXene-Decorated Nanoporous Polyethylene Textile for Passive and Active Personal Precision Heating. *ACS Nano* 2021.
- Wang Q-W, Zhang H-B, Liu J, Zhao S, Xie X, Liu L, et al. Multifunctional and Water-Resistant MXene-Decorated Polyester Textiles with Outstanding Electromagnetic Interference Shielding and Joule Heating Performances. *Adv Funct Mater* 2019;29.
- Xie J, Zhang Y, Dai J, Xie Z, Xue J, Dai K, et al. Multifunctional MoSe(2)@MXene Heterostructure-Decorated Cellulose Fabric for Wearable Thermal Therapy. *Small* 2022:e2205853.
- Rodrigues M-T-F, Babu G, Gullapalli H, Kalaga K, Sayed FN, Kato K, et al. A materials perspective on Li-ion batteries at extreme temperatures. *Nat Energy* 2017;2.
- Ma S, Jiang M, Tao P, Song C, Wu J, Wang J, et al. Temperature effect and thermal impact in lithium-ion batteries: A review. *Prog Nat Sci: Mater Int* 2018;28:653–66.
- Kong X, Zhao X, Li C, Jia Z, Yang C, Wu Z, et al. Terminal Group-Oriented Self-Assembly to Controllably Synthesize a Layer-by-Layer SnSe(2) and MXene Heterostructure for Ultrastable Lithium Storage. *Small* 2023;19:e2206563.
- Wandt J, Jakes P, Granwehr J, Eichel R-A, Gasteiger HA. Quantitative and time-resolved detection of lithium plating on graphite anodes in lithium ion batteries. *Mater Today* 2018;21:231–40.
- Wang Z, Kong Q-Q, Yi Z-L, Xie L-J, Jia H, Chen J-P, et al. Electromagnetic interference shielding material for super-broadband: multi-walled carbon nanotube/silver nanowire film with an ultrathin sandwich structure. *J Mater Chem A* 2021;9:25999–6009.
- Zhang J, Li H, Xu T, Wu J, Zhou S, Hang ZH, et al. Homogeneous silver nanoparticles decorating 3D carbon nanotube sponges as flexible high-performance electromagnetic shielding composite materials. *Carbon* 2020;165:404–11.
- Zhang H, Zhang G, Gao Q, Zong M, Wang M, Qin J. Electrically electromagnetic interference shielding microcellular composite foams with 3D hierarchical graphene-carbon nanotube hybrids. *Compos A Appl Sci Manuf* 2020;130.
- Yu I, Ko J, Kim T-W, Lee DS, Kim ND, Bae S, et al. Effect of sorted, homogeneous electronic grade single-walled carbon nanotube on the electromagnetic shielding effectiveness. *Carbon* 2020;167:523–9.
- Xue B, Li Y, Cheng Z, Yang S, Xie L, Qin S, et al. Directional Electromagnetic Interference Shielding Based on Step-Wise Asymmetric Conductive Networks. *Nanomicro Lett* 2021;14:16.
- Cheng M, Ying M, Zhao R, Ji L, Li H, Liu X, et al. Transparent and Flexible Electromagnetic Interference Shielding Materials by Constructing Sandwich AgNW@MXene/Wood Composites. *ACS Nano* 2022;16:16996–7007.
- Deng Z, Li L, Tang P, Jiao C, Yu ZZ, Koo CM, et al. Controllable Surface-Grafted MXene Inks for Electromagnetic Wave Modulation and Infrared Anti-Counterfeiting Applications. *ACS Nano* 2022;16:16976–86.
- Feng L, Wei P, Song Q, Zhang J, Fu Q, Jia X, et al. Superelastic, Highly Conductive, Superhydrophobic, and Powerful Electromagnetic Shielding Hybrid Aerogels Built from Orthogonal Graphene and Boron Nitride Nanoribbons. *ACS Nano* 2022;16:17049–61.
- Yao B, Hong W, Chen T, Han Z, Xu X, Hu R, et al. Highly Stretchable Polymer Composite with Strain-Enhanced Electromagnetic Interference Shielding Effectiveness. *Adv Mater* 2020;32:e1907499.
- Chen Z, Xu C, Ma C, Ren W, Cheng HM. Lightweight and flexible graphene foam composites for high-performance electromagnetic interference shielding. *Adv Mater* 2013;25:1296–300.
- Crespo M, González M, Elías AL, Pulickal Rajukumar L, Baselga J, Terrones M, et al. Ultra-light carbon nanotube sponge as an efficient electromagnetic shielding material in the GHz range, *physica status solidi (RRL)* - Rapid Research Letters 2014;8:698–704.
- Jia LC, Zhang G, Xu L, Sun WJ, Zhong GJ, Lei J, et al. Robustly Superhydrophobic Conductive Textile for Efficient Electromagnetic Interference Shielding. *ACS Appl Mater Interfaces* 2019;11:1680–8.

- [47] Ling J, Zhai W, Feng W, Shen B, Zhang J, Zheng W. Facile preparation of lightweight microcellular polyetherimide/graphene composite foams for electromagnetic interference shielding. *ACS Appl Mater Interfaces* 2013;5:2677–84.
- [48] Song Q, Ye F, Yin X, Li W, Li H, Liu Y, et al. Carbon Nanotube-Multilayered Graphene Edge Plane Core-Shell Hybrid Foams for Ultrahigh-Performance Electromagnetic-Interference Shielding. *Adv Mater* 2017;29.
- [49] Sun R, Zhang H-B, Liu J, Xie X, Yang R, Li Y, et al. Highly Conductive Transition Metal Carbide/Carbonitride(MXene)/polystyrene Nanocomposites Fabricated by Electrostatic Assembly for Highly Efficient Electromagnetic Interference Shielding. *Adv Funct Mater* 2017;27.
- [50] Sun X, Liu X, Shen X, Wu Y, Wang Z, Kim J-K. Graphene foam/carbon nanotube/poly(dimethyl siloxane) composites for exceptional microwave shielding. *Compos A Appl Sci Manuf* 2016;85:199–206.
- [51] Zeng Z, Jin H, Chen M, Li W, Zhou L, Zhang Z. Lightweight and Anisotropic Porous MWCNT/WPU Composites for Ultrahigh Performance Electromagnetic Interference Shielding. *Adv Funct Mater* 2016;26:303–10.
- [52] Zhang H-B, Zheng W-G, Yan Q, Jiang Z-G, Yu Z-Z. The effect of surface chemistry of graphene on rheological and electrical properties of polymethylmethacrylate composites. *Carbon* 2012;50:5117–25.
- [53] Ameli A, Nofar M, Wang S, Park CB. Lightweight polypropylene/stainless-steel fiber composite foams with low percolation for efficient electromagnetic interference shielding. *ACS Appl Mater Interfaces* 2014;6:11091–100.
- [54] Han M, Yin X, Wu H, Hou Z, Song C, Li X, et al. Ti3C2 MXenes with Modified Surface for High-Performance Electromagnetic Absorption and Shielding in the X-Band. *ACS Appl Mater Interfaces* 2016;8:21011–9.
- [55] Li H, Jing L, Ngoh ZL, Tay RY, Lin J, Wang H, et al. Engineering of High-Density Thin-Layer Graphite Foam-Based Composite Architectures with Superior Compressibility and Excellent Electromagnetic Interference Shielding Performance. *ACS Appl Mater Interfaces* 2018;10:41707–16.
- [56] Li Y, Pei X, Shen B, Zhai W, Zhang L, Zheng W. Polyimide/graphene composite foam sheets with ultrahigh thermostability for electromagnetic interference shielding. *RSC Adv* 2015;5:24342–51.
- [57] Pande S, Chaudhary A, Patel D, Singh BP, Mathur RB. Mechanical and electrical properties of multiwall carbon nanotube/polycarbonate composites for electrostatic discharge and electromagnetic interference shielding applications. *RSC Adv* 2014;4.
- [58] Verma P, Saini P, Malik RS, Choudhary V. Excellent electromagnetic interference shielding and mechanical properties of high loading carbon-nanotubes/polymer composites designed using melt recirculation equipped twin-screw extruder. *Carbon* 2015;89:308–17.
- [59] Yan D-X, Pang H, Li B, Vajtai R, Xu L, Ren P-G, et al. Structured Reduced Graphene Oxide/Polymer Composites for Ultra-Efficient Electromagnetic Interference Shielding. *Adv Funct Mater* 2015;25:559–66.
- [60] Yang Y, Gupta MC, Dudley KL, Lawrence RW. Novel Carbon Nanotube–Polystyrene Foam Composites for Electromagnetic Interference Shielding. *Nano Lett* 2005;5:2131–4.